nature communications

Article

https://doi.org/10.1038/s41467-025-61587-3

Rab27a regulates the transport of influenza virus membrane proteins to the plasma membrane

Received: 21 March 2024

Accepted: 25 June 2025

Published online: 08 July 2025

Check for updates

Tong Chen[1,5], Aotian Ouyang[1,5], Jiahui Zou[1], Yi Feng[1], Changsong Wu[1], Meijun Jiang[1], Shaoyu Tu[1], Ling Ding[1], Yanqing Cheng[1], Wenshuo Hu[1], Wei Sheng[1], Yanglin Li[1], Meilin Jin[1,2], Huanchun Chen[1,2,3,4] & Hongbo Zhou[1,2,3,4]

The molecular mechanisms underlying the transport of influenza A virus (IAV) membrane proteins to the cell surface remain largely unclear. In this study, siRNA screening identifies Rab27a as a critical host factor regulating this transport process. GTP-bound Rab27a operates via its effectors, synaptotagmin-like protein 1 (SYTL1) and SYTL4, to facilitate the transport of vesicles carrying viral membrane proteins to the plasma membrane. Absence of Rab27a or SYTL4 does not block the early stages of the IAV life cycle but restricts viral assembly and budding. Notably, silencing SYTL4 provides superior protection in the female mouse IAV infection model. This investigation elucidates the molecular mechanism by which Rab27a and its effectors modulate the transport of IAV membrane proteins, thereby bridging a critical gap in IAV life cycle research and presenting a potential target for the development of antiviral drugs.

Influenza A virus (IAV) is an enveloped negative-stranded RNA virus responsible for seasonal epidemics, causing approximately 290,000–650,000 deaths annually[1]. Virion assembly and budding at the host cell surface are the final steps of IAV life cycle and are essential for producing infectious particles. The enrichment of influenza A virus membrane proteins (including Hemagglutinin (HA), Neuraminidase (NA), and Matrix Protein 2 (M2)) and the positioning of viral ribonucleoprotein (vRNP) complexes at budding sites are prerequisites for triggering budding[2]. While numerous studies have demonstrated that the host factor Rab11a, associated with recycling endosomes, guides the transport of vRNP to the budding sites[3–6], the molecular mechanism regulating the transport of viral membrane proteins to these sites remain unclear.

It is known that most membrane proteins are transported through secretory vesicles or tubular structure to plasma membrane from the Golgi network[7]. This process mainly regulated by sorting proteins, Rab GTPases, motor proteins, and SNARE complexes. Among these, Rab GTPases rely on their effectors to coordinate the functioning of other proteins[8]. The Rab GTPase family, the largest subgroup within the small GTPase superfamily, comprises over 70 members in humans, with protein sizes ranging from 21 to 25 kDa and localized to distinct intracellular membranes[9]. The regulatory functions of Rab GTPases necessitate a cyclic transformation between an inactive, GDP-bound form and an active, GTP-bound form, with only the latter capable of recruiting specific effectors to mediate diverse functions[9]. Therefore, identifying Rab GTPases involved in post-Golgi transport is anticipated to reveal key host factors participating in the transport of IAV membrane proteins.

In this study, we employed siRNAs targeting Rab GTPases involved in post-Golgi transport to identify the critical host factor capable of reducing the cell surface distribution of HA during IAV infection. We found that GTP-bound form of Rab27a facilitates IAV assembly and budding by mediating the transport of viral membrane proteins to the cell surface. Using the RUSH (retention using selective hooks) system, we visualized the transport pathway of HA and clarified

[1]National Key Laboratory of Agricultural Microbiology, College of Veterinary Medicine, Huazhong Agricultural University, Wuhan, P.R. China. [2]Frontiers Science Center for Animal Breeding and Sustainable Production, Wuhan, P.R. China. [3]Hubei Hongshan Laboratory, Wuhan, P.R. China. [4]Key Laboratory of Preventive Veterinary Medicine in Hubei Province, the Cooperative Innovation Center for Sustainable Pig Production, Wuhan, P.R. China. [5]These authors contributed equally: Tong Chen, Aotian Ouyang. e-mail: hbzhou@mail.hzau.edu.cn

that Rab27a regulates its transport to the plasma membrane via Rab27a positive vesicles. Furthermore, Rab27a depends on its effectors, SYTL1 and SYTL4, to function in viral infection. Notably, silencing SYTL4 provided a higher protection rate against IAV infection in mice than silencing Rab27a. In summary, our study elucidates the role of Rab27a and its effectors SYTL1 and SYTL4 in the transport of influenza virus membrane proteins to the plasma membrane, bridging a crucial gap in our understanding of IAV's life cycle and offering a potential target for antiviral drug development.

Results

Rab27a promotes IAV replication

To avoid potential confounding effects of multiple rounds of viral replication during the screening, we first determined that the budding time of HM virus in A549 cells was between 3 and 4 h post-infection (hpi) (Supplementary Fig. 1a). To identify Rab GTPases that participate in IAV membrane protein transport, we silenced nine Rab GTPases involved in post-Golgi vesicle transport in A549 cells using effective siRNAs (Supplementary Fig. 1b–j) and subsequently infected the cells with HM virus at a high multiplicity of infection (MOI, 10). Among them, Rab27a knockdown significantly reduced HA protein levels on the cell surface at 4 hpi, indicating its crucial role in the transport of IAV membrane proteins (Fig. 1a). Further, efficient and non-cytotoxic siRNA-mediated knockdown of Rab27a markedly decreased intracellular NP levels and reduced the release of infectious viral particles at 24 hpi (Fig. 1b and Supplementary Fig. 1k).

Rab27 has two isoforms, Rab27a and Rab27b, that share 71% identity[10]. To explore whether Rab27b is also involved in viral membrane protein transport, we generated Rab27a knockout (KO), Rab27b KO, and Rab27a and Rab27b double-knockout (Rab27-DK) monoclonal cells (Supplementary Fig. 1l–n), and examined replication and HA surface distribution in these cells after infection. Rab27b KO moderately impaired IAV replication and HA surface levels, while Rab27a KO had a more pronounced effect. The most significant reductions were observed in Rab27-DK cells, indicating that both isoforms regulate HA transport, with Rab27a playing a dominant role (Supplementary Fig. 1o, p). Subsequent experiments, therefore, focused on Rab27a.

We next examined the effect of Rab27a on the replication of various IAV subtypes, including HM, SH13, and PR8. Rab27a KO significantly impaired the replication of all tested subtypes (Fig. 1c–e). This effect was Rab27a-specific, as complementation of synonymous mutant HA-Rab27a plasmid in Rab27a KO cells increased the virus titer compared with the empty vector group (Supplementary Fig. 1q). Conversely, ectopic expression of Rab27a significantly enhanced viral titers and intracellular NP levels of all tested subtypes in A549 cells (Fig. 1f–h).

In addition, we stably expressed wild-type Rab27a (Rab27a-WT), a constitutively active mutant (Rab27a-Q78L), and a dominant-negative mutant (Rab27a-T23N) in Rab27a KO cells. At 24 hpi, the viral titers in cells expressing the active form of Rab27a were higher than those in cells expressing the wild-type Rab27a protein, whereas the titers in cells expressing the inactive form were comparable to those in Rab27a KO cells, suggesting that the GTP-bound form of Rab27a plays a dominant role in IAV replication (Fig. 1i). Taken together, these data provide strong evidence that Rab27a facilitates the replication of various IAV subtypes and serves a critical role in the viral life cycle.

Knocking out Rab27a restricts IAV assembly and budding

IAV infects host cells via endocytosis, and is transported from early to late endosomes, where vRNPs are released and transported into the nucleus for transcription and replication[11,12]. Newly synthesized viral genomes and proteins are then assembled into virions on the cell surface for release[13,14]. Since Rab27a is partially localized to late endosomes[10], we investigated whether it might be involved in the early stages of IAV infection. Co-localization analysis of NP with DAPI revealed no significant differences between Rab27a-KO cells and A549-Cas9 cells at 0.5 and 1 hpi (Fig. 2a). It indicated that Rab27a KO does not affect nuclear entry of vRNP or the preceding stages of the IAV life cycle, including adsorption, internalization, and membrane fusion.

We proceeded to investigate whether Rab27a affects IAV primary transcription and replication. The results showed that Rab27a KO did not affect the mRNA levels of the viral structural proteins at 4 hpi, with or without Cycloheximide (CHX, a protein synthesis inhibitor)[15] treatment (Fig. 2b, c), suggesting that Rab27a did not participate in primary transcription or replication. Notably, while the vRNA levels of these viral proteins were similar between Rab27a-KO and A549-Cas9 cells at 3 hpi, they were significantly higher in Rab27a-KO cells at 4 hpi (Fig. 2d, e), which coincides with the time point of virion budding (Supplementary Fig. 1a). These findings suggest that in Rab27a-KO cells, more vRNP is retained and fails to participate in the assembly of viral particles.

Subsequently, we examined the budding of IAV in A549-Cas9 cells, Rab27a-KO cells, and Rab27a-KO cells stably expressing Rab27a-WT, Rab27a-T23N, or Rab27a-Q78L at 6 hpi. Statistical analysis showed that viral budding events in Rab27a-KO cells were significantly fewer than those in A549-Cas9 cells (Fig. 2f). Furthermore, Rab27a-Q78L-expressing cells exhibited a higher number of budding events compared to Rab27a-WT-expressing cells. Rab27a-T23N-expressing cells displayed a budding frequency comparable to that of Rab27a-KO cells, but lower than Rab27a-WT-expressing cells (Fig. 2f). Taken together, these data indicate that while Rab27a does not participate in the early stages of viral infection, its GTP-bound form plays a critical role in the assembly and budding of IAV.

Rab27a regulates transport of HA and NA proteins to plasma membrane

Given that high concentrations of membrane protein are required on host-cell membranes for virion assembly, we speculated that Rab27a regulates IAV assembly and budding by mediating the transport of viral membrane proteins. Supporting this, at the late stage of infection, Rab27a-KO cells released fewer virions (Fig. 1c–e), but at the early stage of infection, they exhibited significantly higher intracellular levels of structural proteins, particularly viral membrane proteins, compared to A549-Cas9 cells (Fig. 3a, b). Moreover, flow cytometry analysis revealed that total levels of viral membrane proteins were higher in Rab27a-KO cells at 6 hpi (Fig. 3c–e), but the surface levels of HA and NA in Rab27a-KO cells were reduced to 70% and 61% of those in A549-Cas9 cells, respectively (Fig. 3f, g). Interestingly, surface levels of M2 in Rab27a-KO cells remained higher than those in A549-Cas9 cells (Fig. 3h), possibly due to differences in the transport mechanisms of M2 compared to HA/NA. These findings were further confirmed by immunofluorescence analysis (Fig. 3i–k). To investigate the role of Rab27a variants in HA transport, we measured cell surface HA levels at 6 hpi in A549-Cas9 cells, Rab27a-KO cells, and Rab27a-KO cells stably expressing Rab27a-WT, Rab27a-T23N, or Rab27a-Q78L. HA levels in Rab27a-T23N-expressing cells were comparable to those in Rab27a-KO cells; both were significantly lower than those in Rab27a-WT- and Rab27a-Q78L-expressing cells (Fig. 3l, m). This result further supported by immunofluorescence analysis (Supplementary Fig. 2a).

To investigate whether Rab27a specifically regulates the transport of influenza virus membrane proteins, we examined its effect on the transport of another representative viral membrane protein, VSV G[16,17]. We first confirmed that VSV G was synthesized starting at 3 hpi and became detectable on the cell surface at 4 hpi (Supplementary Fig. 2b, c). Next, we found no significant differences in either the total or cell surface protein levels of VSV-G between the siRab27a and siNC groups at 4 hpi (Fig. 3n, o). Consistently, silencing Rab27a did not affect the viral titer of VSV-GFP at 24 hpi (Supplementary Fig. 2d, e). In contrast, silencing Rab6a significantly reduced the level of VSV G protein on the cell membrane (Supplementary Fig. 2f), but had no significant effect on the total protein level (Supplementary Fig. 2g). Collectively, these

https://doi.org/10.1038/s41467-025-61587-3

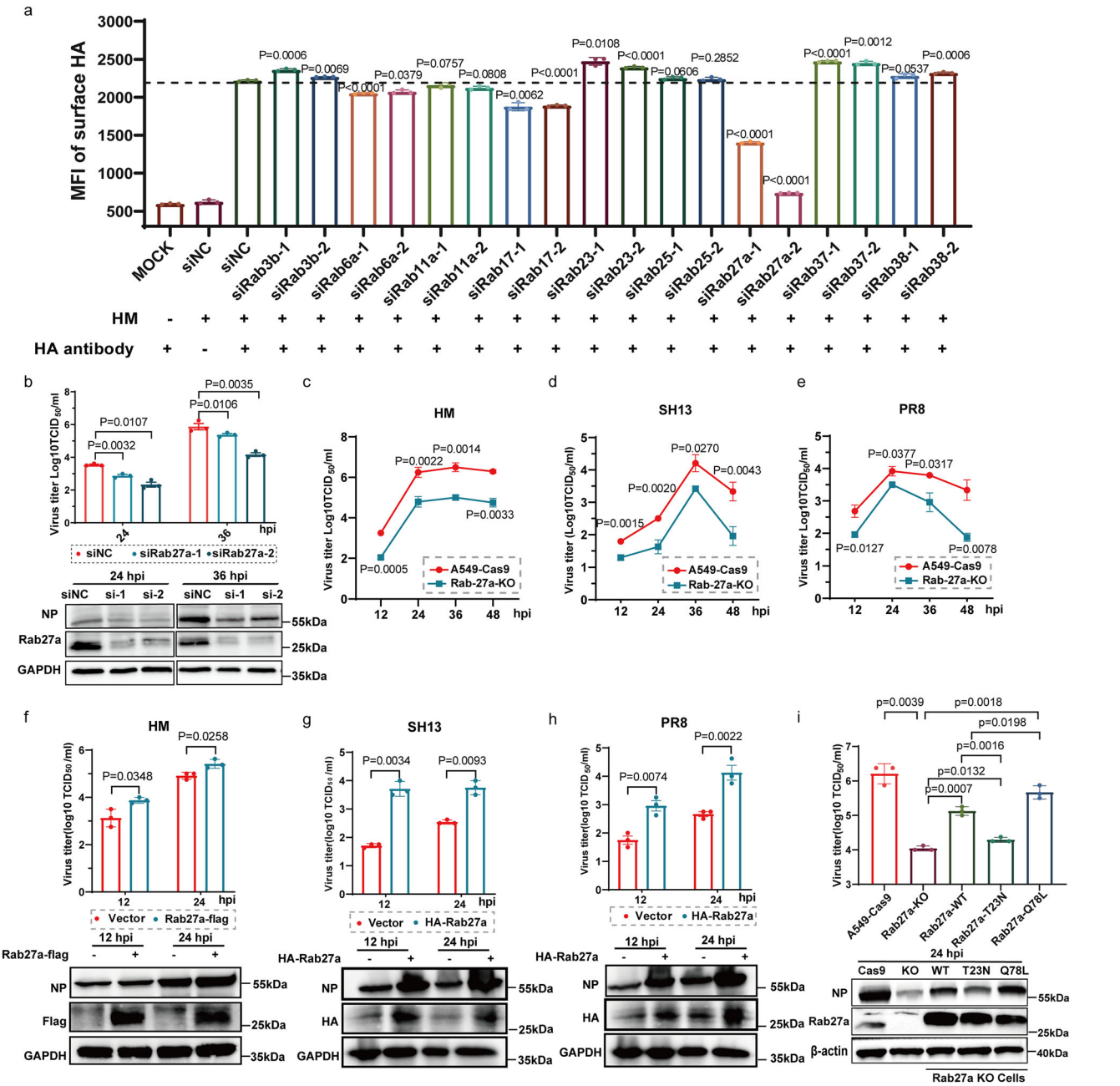

Fig. 1 | Rab27a promotes IAV replication. a A549 cells were transfected with siNC or siRNAs targeting Rab3b (siRab3b-1, siRab3b-2), Rab6a (siRab6a-1, siRab6a-2), Rab11a (siRab11a-1, siRab11a-2), Rab17 (siRab17-1, siRab17-2), Rab23a (siRab23a-1, siRab23a-2), Rab25 (siRab25-1, siRab25-2), Rab27a (siRab27a-1, siRab27a-2), Rab37 (siRab37-1, siRab37-2), or Rab38 (siRab38-1, siRab38-2) for 24 h. The cells were then infected with HM virus (MOI, 10), and HA protein levels on the cell surface were quantified by flow cytometry at 4 hpi. **b** A549 cells transfected with siNC or siRab27a (siRab27a-1, siRab27a-2) for 24 h were infected with HM virus (MOI, 0.1). **c**–**e** Rab27a KO and A549-Cas9 cells were infected with HM virus (MOI, 0.1), SH13/H9N2 virus (MOI, 0.01), or PR8/H1N1 virus (MOI, 0.01). **f**–**h** A549 cells were transfected with 2 μg/ml exogenous Rab27a or an empty vector as a negative control for 24 h. The cells were then infected with HM virus (MOI, 0.1), SH13 virus (MOI, 0.01), or PR8 virus (MOI, 0.01). **i** A549-Cas9, Rab27a KO, and Rab27a KO cells stably expressing Flag-Rab27a-WT, Flag-Rab27a-T23N (dominant-negative mutant), or Flag-Rab27a-Q78L (constitutively active mutant) were infected with HM virus (MOI, 0.1). Rab27a and NP protein expression levels were examined by western blot (**b**, **f**, **g**, **h**, and **i**), with GAPDH or β-actin serving as a loading control. Viral titers in the supernatants were quantified using a $TCID_{50}$ assay on MDCK cells (**b**–**i**). Data represent the means ± SD from three independent experiments. Statistical significance was determined using a two-tailed Student's *t*-test.

data suggest that GTP-bound form of Rab27a specifically regulates the transport of HA and NA to the plasma membrane.

Rab27a promotes autophagy and M2 transport to plasma membrane

In the previous section, we observed that the distribution of M2 on the cell surface was increased following Rab27a KO (Fig. 3h, k). We further confirmed that M2 can be degraded through autophagy pathway (Supplementary Fig. 3a). Given that M2 localizes to autophagosomes and induces incomplete autophagy[18,19], we hypothesized that Rab27a KO might impair autophagy, leading to abnormal accumulation of M2 on the cell surface. Supporting this hypothesis, Rab27a overexpression increased LC3B-II levels during viral infection, especially with Bafilomycin A1 (BafA1) treatment, indicating enhanced autophagy initiation

https://doi.org/10.1038/s41467-025-61587-3

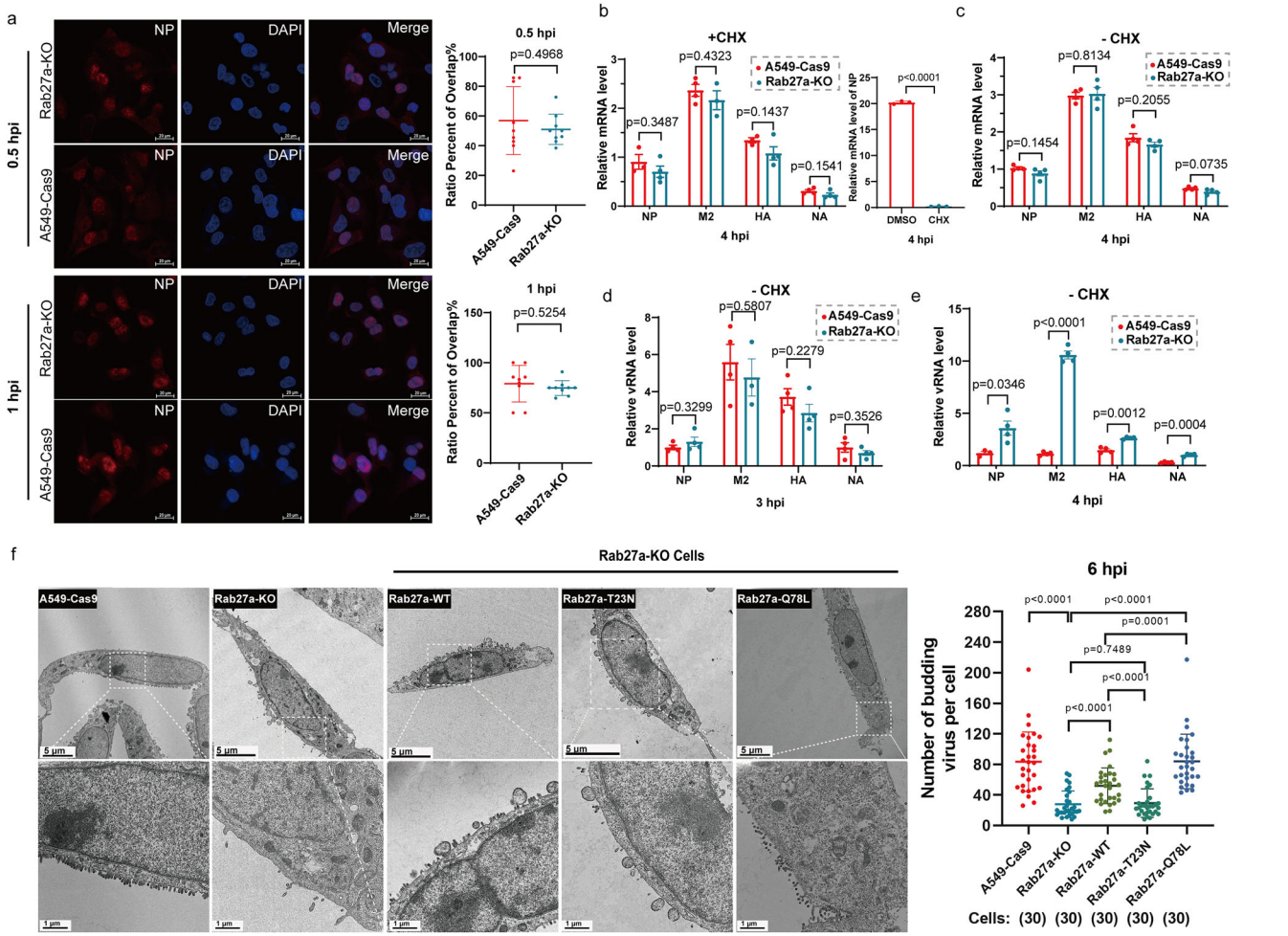

Fig. 2 | Knocking out Rab27a restricts IAV assembly and budding. a Rab27a-KO and A549-Cas9 cells were infected with HM virus (MOI, 10). At 0.5 and 1 hpi, cells were fixed, permeabilized, and stained with anti-NP (red) and DAPI (blue). At least 9 randomly selected fields from each group were analyzed for quantitative co-localization of the nucleus and NP protein. Representative images are shown in (**a**). Scale bar, 20 μm. Data represent the mean ± SD from one representative experiment of at least three independent experiments, with at least 100 cells per condition quantified. **b**–**e** Rab27a-KO and A549-Cas9 cells were pretreated with cycloheximide (CHX, 100 μM) or DMSO (−CHX) for 4 h, followed by infection with HM virus (MOI, 10) and subsequent treatment with CHX (350 μM) or DMSO. The mRNA and vRNA levels of viral genes were quantified by qRT-PCR and normalized to 18S rRNA levels. **f** A549-Cas9, Rab27a-KO, and Rab27a-KO cells stably expressing Flag-Rab27a-WT, Flag-Rab27a-T23N, or Flag-Rab27a-Q78L were infected with HM virus (MOI, 10). Cells were fixed in glutaraldehyde at 6 hpi, and the budding of influenza viruses was observed using transmission electron microscopy (TEM). For quantitative analysis, 30 cells were randomly selected from each group to determine the number of IAV budding events. Representative images are shown in (**f**), with scale bars of 5 μm and 1 μm. Data represent the mean ± SD from one representative experiment of at least three independent experiments. Statistical significance was analyzed using a two-tailed Student's *t*-test.

(Fig. 4a). Conversely, Rab27a KO reduced LC3B-II levels under infection and treatment with BafA1, and decreased the punctate distribution of LC3-GFP under starvation, further suggesting that Rab27a promotes autophagy (Fig. 4b, c).

To elucidate how Rab27a facilitates autophagy, autophagy-related genes (ATGs) protein levels were evaluated in both Rab27a-KO and A549-Cas9 cells at 6 and 12 hpi, and remarkable change was observed in ATG4B level (Fig. 4d). A complex involving ATG4B, LC3, and Rab27a was predicted by molecular modeling, suggesting a strong interaction between Rab27a (orange) and the ATG4B (golden)-LC3 (green) complex. Notably, the phosphorylation site, serine 316 (Ser316, red), of ATG4B is located at the center of the complex (Fig. 4e). Subsequent co-immunoprecipitation validation confirmed the interaction between Rab27a and ATG4B (Fig. 4f, g). Previous studies reported that ULK1 inhibits LC3 processing by phosphorylating ATG4B at Ser316[20]. Based on this, we hypothesized that Rab27a appeared to shield Ser316 from phosphorylation by ULK1, promoting autophagy. Supporting this, Rab27a KO reduced ATG4B levels while increasing Ser316 phosphorylation, whereas Rab27a overexpression had the opposite effect (Fig. 4h, i). These results have shown that Rab27a's promotion of autophagy was more pronounced under viral infection, which might be related to M2. In this context, we further to detect the role of M2 in Rab27a-mediated autophagy. The results showed that co-expression of Rab27a with M2 more effectively inhibited Ser316 phosphorylation of ATG4B and increased LC3-I levels, with significant co-localization of M2, Rab27a, and LC3 observed via confocal microscopy (Fig. 4j, k).

Given the significant co-localization of M2 with Rab27a, we further examined whether M2 influences Rab27a protein expression or stability. Overexpression of M2 significantly increased Rab27a protein levels (Supplementary Fig. 3b), and treatment with autophagy inhibitors (CQ, 3-MA) and proteasome inhibitors (MG132) restored the Rab27a protein level in cells co-transfected with an empty vector (Supplementary Fig. 3c, d), suggesting that M2 enhances stabilization of Rab27a protein through both autophagy and proteasome pathways. Since these pathways target ubiquitinated proteins, we hypothesized that M2 reduces Rab27a ubiquitination to stabilize its protein levels

https://doi.org/10.1038/s41467-025-61587-3

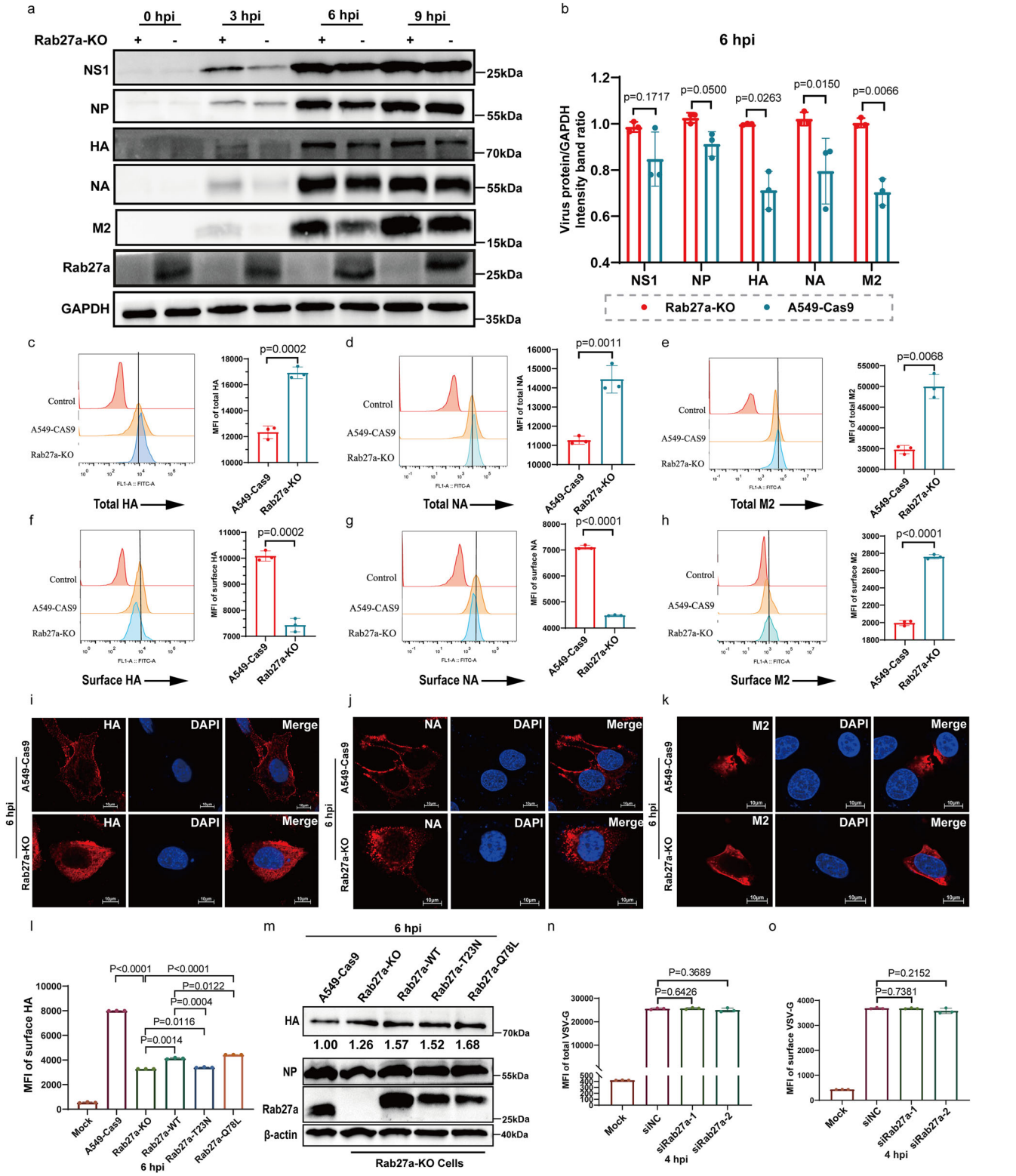

and promote viral replication. Indeed, co-transfection with M2 significantly decreased Rab27a ubiquitination, as shown by anti-ubiquitin immunoblotting (Supplementary Fig. 3e).

Lastly, we investigated whether Rab27a regulates the transport of M2 to the cell surface. Flow cytometry revealed that Rab27a overexpression did not alter total M2 protein levels but significantly increased its surface levels, indicating that Rab27a facilitates M2 transport to the plasma membrane (Fig. 4l). In conclusion, these findings demonstrate that Rab27a promotes autophagy, and the elevated M2 levels on the surface of Rab27a-KO cells result from decreased autophagy. Importantly, Rab27a also directly regulates M2 transport to the cell surface.

Rab27a regulates the transport of viral membrane proteins to the plasma membrane through Rab27a positive vesicles

To elucidate the specific pathway of Rab27a regulating the transport of influenza virus membrane proteins, we first measured the effect of Rab27a KO on co-localizations of HA proteins with the membrane-

Fig. 3 | Rab27a regulates transport of HA and NA proteins to apical plasma membrane. a Rab27a-KO and A549-Cas9 cells were infected with HM virus (MOI, 10). Rab27a and viral protein levels were analyzed by western blot at 0, 3, 6, and 9 hpi, with GAPDH serving as a loading control. **b** Western blot densitometry at 6 hpi analysis was performed using ImageJ software. **c**–**h** Rab27a-KO and A549-Cas9 cells were infected with HM virus (MOI, 10). At 6 hpi, total (permeabilized) and cell surface (nonpermeabilized) levels of viral membrane proteins were quantified by flow cytometry. The bar graph shows the MFI. **i**–**k** Rab27a-KO and A549-Cas9 cells were infected with HM virus (MOI, 10). At 6 hpi, cells were fixed, permeabilized, and stained with antibodies against HA, NA, and M2 (all in red) and DAPI (blue). Scale bar, 10 μm. **l**, **m** A549-Cas9, Rab27a-KO, and Rab27a-KO cells stably expressing Flag-Rab27a-WT, Flag-Rab27a-T23N, or Flag-Rab27a-Q78L were infected with HM virus (MOI, 10). At 6 hpi, HA protein levels on the cell surface were quantified by flow cytometry (**l**), while HA, NP, and Rab27a protein levels were analyzed by western blot (**m**), with β-actin serving as a loading control. **n**, **o** A549 cells transfected with siNC or siRab27a (siRab27a-1, siRab27a-2) for 24 h were infected with VSV (MOI, 10). Total (**n**) and cell surface (**o**) levels of VSV-G protein were quantified by flow cytometry. Data are presented as mean ± SD from three independent experiments. Statistical significance was determined using a two-tailed Student's *t*-test.

bound organelles that they might pass through. The results showed that there were no significant differences in the co-localizations of HA with different organelles (including cis-Golgi, trans-Golgi, and late endosomes) between Rab27a KO and A549-Cas9 cells under infection conditions (Fig. 5a–c). Therefore, we speculate that the step where Rab27a functions may be the secretory vesicles of the Golgi apparatus. The RUSH (retention using selective hooks) system[21] utilizes the streptavidin-binding peptide (SBP) binds streptavidin with high affinity and can be outcompeted by biotin, enabling synchronous release of viral proteins from the endoplasmic reticulum (ER, anchored by Li) or Golgi (anchored by Golgin-84) as shown in Fig. 5d. These help to visualize the transport pathway of viral membrane proteins and confirm the specific steps in which Rab27a is involved. After biotin addition, we observed that most of the HA protein anchored to the ER in A549 cells can reach the cis-Golgi at 20 min, the trans-Golgi at 30 min, and the cell surface at about 90 min, but not co-located with late endosomes. Therefore, we chose to delay the above time by 10–15 min to observe the effect of Rab27a KO on HA transport. The results showed that there were no significant differences in the co-localizations of HA with the cis-Golgi and trans-Golgi between Rab27a KO and A549-Cas9 cells, but the proportion of HA proteins on the cell surface was lower in Rab27a KO cells (Fig. 5e–h). Importantly, we found that at 90 min after biotin addition, a large number of punctate vesicles were retained in the Rab27a KO cells (Fig. 5h), indicating that Rab27a KO prevents the effective transport of these vesicles carrying HA proteins to the plasma membrane. As a control, the proportion of VSV G proteins on the cell surface after the synchronous addition of biotin for 90 min did not decrease in Rab27a KO cells compared with A549-Cas9 cells, further confirming the specificity of Rab27a in regulating the transport of influenza virus membrane proteins to the plasma membrane (Supplementary Fig. 4a). In addition, after synchronous release of M2 anchored by the Golgi for 60 min in Rab27a KO and A549-Cas9 cells, the proportion of M2 protein on the cell surface in Rab27a KO cells was lower, indicating that Rab27a regulates the transport of M2 released from Golgi to the cell surface (Fig. 5i, j). Additional evidence showed that there were no significant differences in the co-localizations of Rab27a with Golgi network or late endosomes before and after infection (Supplementary Fig. 4b–d), but the co-localizations with autophagosomes were increased (Supplementary Fig. 4e), indicating that the subcellular compartments where Rab27a may function after infection are autophagosomes or Rab27a positive vesicles.

To clarify the rationality of Rab27a regulating transport of newly synthesized HA, NA, and M2 proteins, we examined the co-localizations of these proteins with Rab27a. Because Rab27a can localize with endosomes[10] (Supplementary Fig. 4d), and IAV relies on endocytosis to enter cell, whether Rab27a co-locates with viral membrane proteins should be tested under conditions allowing only a single round of viral replication. Therefore, after viral adsorption was completed, we treated these infected cells with oseltamivir, a neuraminidase inhibitor that can block both viral particle release[22] and subsequent adsorption[23,24], then the localizations of Rab27a with newly synthesized viral membrane proteins were detected at 4 hpi, while the infected viral cells were treated with CHX in the control group to distinguish the viral membrane proteins that entered the cells in the first round. Meanwhile, we used 120 μM of oseltamivir to ensure that a new round of viral infection was completely blocked (Supplementary Fig. 4f, g). The results showed that Rab27a co-located with both HA and NA significantly at 4 hpi (white arrow), while no significant localization was observed in the control group (Fig. 5k). Interestingly, HA (yellow arrow) and NA (blue arrow) were also found to colocalize with Rab27a individually (Fig. 5k), indicating that Rab27a regulates the transport of HA and NA in a partially asynchronous manner. In addition, we observed that Rab27a also colocalized with HA and NA in the perinuclear region, which may result from the fact that both Rab27a and the viral proteins undergo synthesis and processing in the ER and Golgi apparatus. To further confirm that the vesicles showing Rab27a–HA/NA colocalization near the plasma membrane had separated from the ER–Golgi network, we examined the localization of these vesicles in relation to the ER and Golgi individually. The results showed that Rab27a–HA/NA colocalization near the plasma membrane did not overlap with either the ER or the Golgi (Supplementary Fig. 4h), indicating that Rab27a-positive vesicles, pinching off from the Golgi or ER, possess the spatial feasibility to mediate the transport of viral proteins to the plasma membrane. Similarly, colocalization of M2 with Rab27a was also observed near the plasma membrane (yellow arrow) (Fig. 5l). Consistently, exogenous Rab27a can also significantly co-localize with exogenous viral proteins (Supplementary Fig. 4i).

Based on the above results of the above two aspects, Rab27a regulates the transport of Rab27a positive vesicles carrying viral membrane proteins to the plasma membrane.

SYTL1 and SYTL4 are two Rab27a effectors involved in IAV membrane protein transport

Rab27a exists in two forms: the active GTP-bound and the inactive GDP-bound forms, with the active form modulating downstream effector proteins[25]. To identify Rab27a effectors involved in IAV infection, we analyzed the mRNA levels of 10 effectors in A549 cells. Among these, the mRNA levels of *SYTL1*, *SYTL2*, *SYTL3*, *SYTL4*, and *SLAC-2b* were significantly increased following IAV infection (Supplementary Fig. 5a). The Rab27a-binding domain (SHD) of these five effectors, GST-SHD fusion proteins, and GST alone were expressed in *E. coli* and purified (Supplementary Fig. 5b)[26]. GST-pulldown assays demonstrated that Rab27a interactions with the SHDs of SYTL1 and SYTL4 were significantly enhanced after IAV infection (Fig. 6a). In addition, the SHDs of SYTL1 and SYTL4 exhibited the strongest affinity for Rab27a-Q78L, followed by Rab27a-WT, with minimal interaction observed for Rab27a-T23N, validating the specificity of these interactions (Fig. 6b). Silencing either SYTL1 or SYTL4 significantly reduced the release of infectious viral particles at 24 hpi (Fig. 6d and Supplementary Fig. 5c, d), while it led to decreased viral membrane protein levels at 6 hpi, without affecting autophagy levels (Fig. 6c). Efficient knockout of SYTL1 and SYTL4 had equivalent effects on the viral titer, viral protein levels, and autophagy levels (Fig. 6e, f and Supplementary Fig. 5e–h). These results suggest that SYTL1 and SYTL4 are also

https://doi.org/10.1038/s41467-025-61587-3

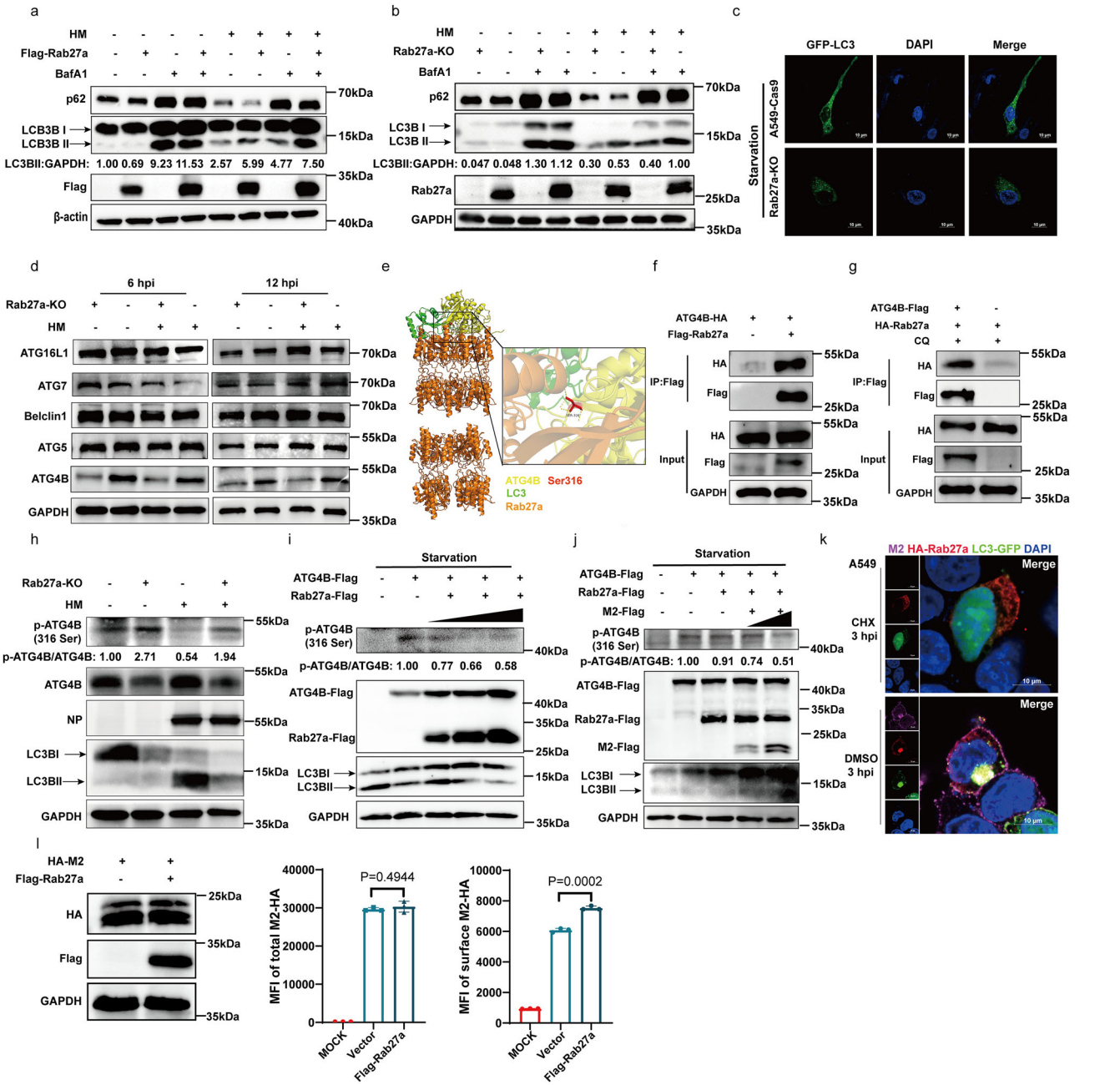

Fig. 4 | Rab27a promotes autophagy and M2 transport to plasma membrane. **a** HEK293T cells were transfected with Rab27a or vector control for 24 h, infected with HM virus (MOI, 0.1) or left uninfected, and treated with BafA1 (400 nM) or DMSO for 24 h. **b** Rab27a-KO and A549-Cas9 cells were infected with HM virus (MOI, 0.1) or left uninfected and treated with BafA1 (400 nM) or DMSO for 24 h. **c** Rab27a-KO and A549-Cas9 cells were transfected with GFP-LC3 for 24 h, followed by starvation treatment for another 24 h. Scale bar, 10 μm. **d** Rab27a-KO and A549-Cas9 cells were infected with HM virus (MOI, 0.1) or left uninfected for 6 and 12 hpi. **e** Molecular modeling predicts complex formation involving ATG4B (golden), Rab27a (orange), and LC3 (green) proteins, highlighting the phosphorylation site serine 316 (Ser316, red) in ATG4B. **f**, **g** HEK293T cells were co-transfected with Rab27a, ATG4B or empty vector for 36 h. co-IP was performed using an anti-Flag antibody (**f**). Cells were treated with CQ (100 μM) (**g**). **h** Rab27a-KO and A549-Cas9 cells were infected with HM virus (MOI, 0.1) or left uninfected for 12 hpi. **i** HEK293T cells were co-transfected with ATG4B and Rab27a or empty vectors. At 24 h post-transfection, cells were subjected to 12 h of starvation. **j** HEK293T cells were co-transfected with ATG4B and Rab27a along with M2 (0, 0.5, or 1 μg/ml) or empty vectors. At 24 h post-transfection, cells were subjected to 12 h of starvation. **k** A549 cells were co-transfected with HA-Rab27a and LC3-GFP for 36 h, pretreated with CHX (100 μM) or DMSO for 4 h, and then infected with HM virus (MOI, 10). Cells were further treated with CHX (350 μM) or DMSO and fixed at 3 hpi. Staining with anti-HA, anti-M2, and DAPI. Scale bar, 10 μm. **l** HEK293T cells were co-transfected with Rab27a, M2 for 24 h. Total and cell surface levels of M2 protein were quantified by flow cytometry. Data are presented as mean ± SD from three independent experiments. Statistical significance was assessed using a two-tailed Student's *t*-test. Western blot analysis was performed for the indicated proteins, with GAPDH or β-actin as a loading control.

involved in the lifecycle of IAV, but their impact on autophagy is different from Rab27a.

Thus, we hypothesized that blocking the transport of viral membrane proteins may lead to their degradation via autophagy. SYTL4 for further validation due to its greater impact on viral replication. Similar to Rab27a KO, SYTL4 KO did not affect viral entry into the nucleus (Fig. 6g) or viral transcription and replication (Fig. 6h, i). However, more viral ribonucleoproteins (vRNPs) were retained in the cytoplasm

https://doi.org/10.1038/s41467-025-61587-3

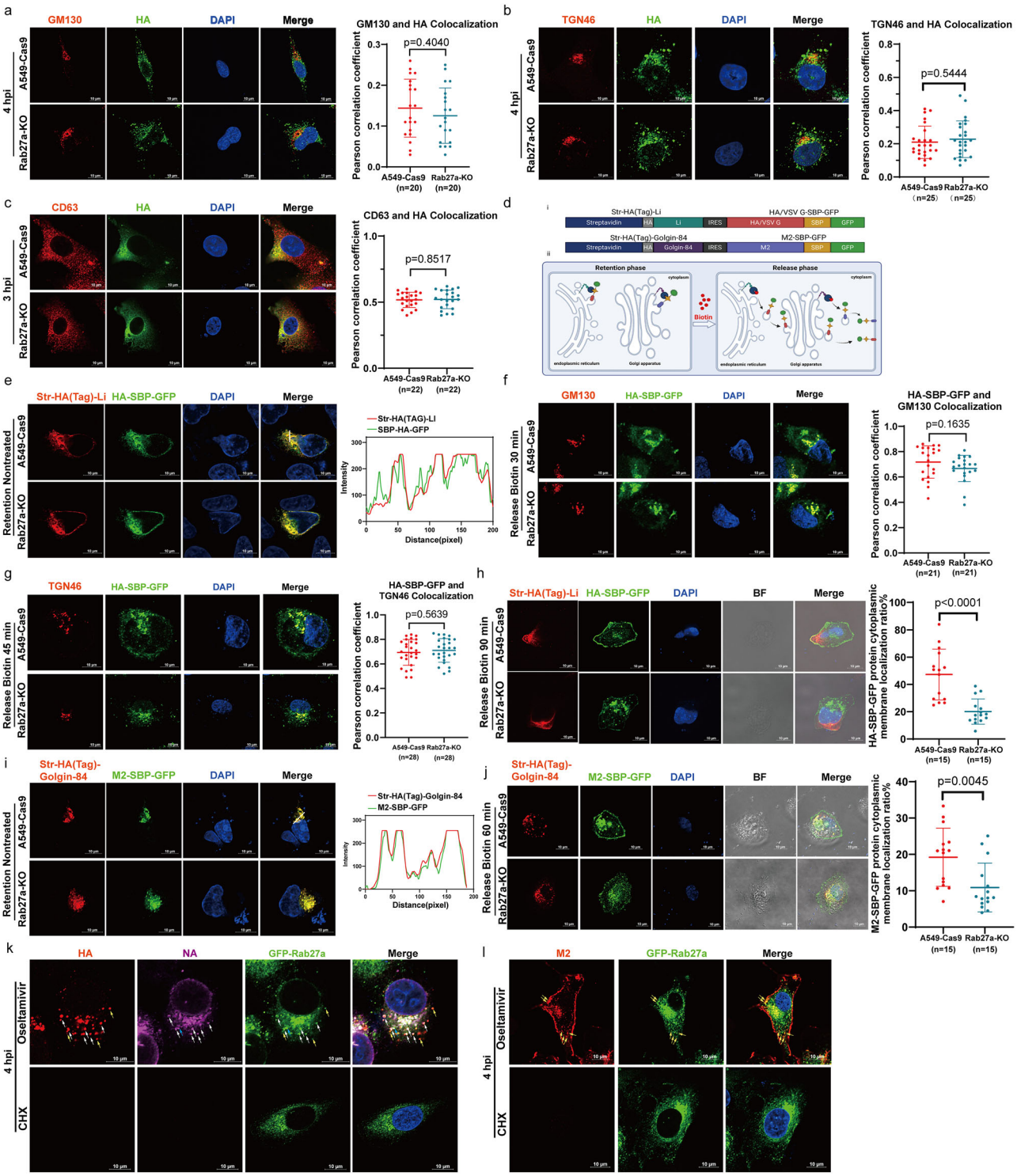

of SYTL4 KO cells compared with A549-Cas9 cells at 4 hpi (Fig. 6j, k), indicating that the assembly and budding of the IAV were inhibited in SYTL4 KO cells. Treatment with the autophagy inhibitor chloroquine (CQ) restored viral membrane protein levels in SYTL4 KO cells to levels comparable to those in A549-Cas9 cells (Fig. 6l), confirming that autophagy-mediated degradation accounted for the reduced viral proteins in SYTL4 KO cells. Next, we measured the cell surface and total protein level of HA and M2 under the same conditions by flow cytometry. The results showed that total levels of HA and M2 in SYTL4 KO cells were higher than those in A549-Cas9 cells under treatment with CQ (Fig. 6m, o), while the cell surface levels of HA and M2 were lower in SYTL4 KO cells (Fig. 6n, p), indicating SYTL4 KO similarly impaired viral proteins transport to the plasma membrane. Moreover, SYTL4 knockdown did not affect the replication of VSV-GFP or VSV G transport, consistent with the Rab27a KO phenotype (Fig. 6q, r and Supplementary Fig. 5k). Overall, these findings indicate that Rab27a relies on its effectors SYTL1 and SYTL4 to specific regulate the transport of viral membrane proteins to the plasma membrane.

SYTL4 is a potential anti-influenza virus drug target

IAV relies entirely on host cells to complete its life cycle, making host factors that are indispensable for viral replication but non-essential for

Fig. 5 | Rab27a regulates the transport of viral membrane proteins to the plasma membrane through Rab27a positive vesicles. a–c Rab27a-KO and A549-Cas9 cells were infected with HM virus (MOI, 10). At 3 (**c**) and 4 hpi (**a**, **b**), cells were stained with anti-GM130, TGN46, CD63, and influenza HA. The co-localization of HA with different organelles was quantified by calculating the Pearson correlation coefficient (PCC) using the Coloc 2 in Fiji. GM130 (**a**, cis-Golgi, $n = 20$); TGN46 (**b**, trans-Golgi, $n = 25$); CD63 (**c**, endosome, $n = 22$). **d** i. Schematic of genes coding for the hook (Str-HA (Tag) -Li/Golgin-84) and the reporter (HA/M2/VSV G-SBP-GFP), expressed under the same CMV promoter, separated by an internal ribosome entry site (IRES); ii. Schematic of the RUSH system. In the absence of biotin, SBP-tagged cargo is retained in the ER or Golgi via interaction with streptavidin-HA (Tag) -Li (ER-localized)/Golgin-84 (Golgi-localized). Addition of biotin disrupts the interaction, allowing forward trafficking of cargo. Image was created in BioRender. Tong, C. (2025) https://BioRender.com/nuf5a1w. **e–j** cells were transfected with Str-HA (Tag) -Li_HA-SBP-GFP or Str-HA (Tag) -Golgin-84_M2-SBP-GFP for 24 h, followed by addition of biotin (400 μM). At corresponding time after biotin addition, cells were stained with anti-HA (Tag), GM130, and TGN46. Co-localizations of M2/HA with ER (**e**, **i**) or proportion of HA/M2 on the cell surface (**h**, **j**, $n = 15$,) was analyzed using Fiji. The co-localization of HA-SBP-GFP with different organelles was also quantified by calculating the PCC. GM130 (**f**, cis-Golgi, $n = 21$); TGN46 (**g**, trans-Golgi, $n = 28$). **k**, **l** A549 cells stably expressing GFP-Rab27a were pretreated with CHX (100 μM) or DMSO for 4 h, and then infected with HM virus (MOI, 10). Cells were further treated with CHX (350 μM) or Oseltamivir (120 μM) and fixed at 4 hpi. In (**k**), staining with anti-HA, anti-NA, and DAPI. In (**l**), staining with anti-M2 and DAPI. White arrows indicate colocalization of HA, NA, and GFP-Rab27a; blue arrows indicate colocalization of NA and GFP-Rab27a; yellow arrows indicate colocalization of HA and GFP-Rab27a in (**k**), and of M2 and GFP-Rab27a in (**l**). Scale bar, 10 μm. Representative images are shown in (**a–c**, **e–l**). Data are presented as mean ± SD from three independent experiments. Statistical significance was assessed using a two-tailed Student's *t*-test.

the host promising targets for antiviral drug development. Our findings demonstrated that Rab27a and SYTL4 are essential for transporting viral membrane proteins, with their silencing inhibiting IAV replication in vitro. To explore their roles in vivo, siRNAs targeting mouse Rab27a and SYTL4 were designed and validated in BHK cells (Supplementary Fig. 6), and the most effective siRNA-3 for each was selected for subsequent experiments, as outlined in Fig. 7a. Silencing efficiencies were confirmed by measuring target protein levels in lung tissue, demonstrating stability and potency (Fig. 7b, c). The body weight losses (Fig. 7d) and survival rates (Fig. 7e) of the si-Rab27a- and si-SYTL4-treated groups demonstrated that knockdown of Rab27a and SYTL4 in vivo contributed to slow down the degree of weight loss, and provided protection rates of 20% and 70%, respectively. H&E staining of mouse lungs showed moderate to severe necrotizing bronchiolitis and alveolitis with focal areas of acute alveolar necrosis, edema, and hemorrhage in the siNC group at 3 dpi and 5 dpi. In contrast, only slight pneumorrhagia and a gradual thickening trend were observed in the siRab27a and siSYTL4 group (Fig. 7f).

Further analysis showed decreased NP protein fluorescence signals and significantly lower viral titers in the lungs of siRab27a- and siSYTL4-treated mice compared to the siNC group at 3 and 5 dpi (Fig. 7g, h). These results suggested that silencing Rab27a and SYTL4 decreased the replication of IAV in vivo, alleviated the lung damage, and decreased IAV-induced mortality in mice. Importantly, the antiviral effect of silencing SYTL4 is superior to Rab27a. Therefore, SYTL4 represents a potential target for developing anti-influenza therapeutics.

Discussion

This study focused on the Rab GTPase family, which plays a key role in regulating membrane protein transport, as the target for screening, and yielding significant insights. Previous research has shown that although Rab8 and Rab26 are involved in vesicle transport during post-Golgi processing, Rab8 does not participate in HA transport[27], and Rab26 restricts insulin exocytosis and inhibits the maturation and release of secretory vesicles in *Drosophila*[28]. Therefore, these two Rab GTPases were excluded from the screening. Interestingly, although Rab11a regulates the transport of vRNP, it does not affect the transport of HA. This observation supports the notion that the accumulation of HA-rich plasma membrane microdomains is a prerequisite for vRNP engagement in virion budding[2].

A previous study showed that the influenza virus HA protein can colocalize with Rab17 and Rab23, and that overexpression of dominant-negative (DN) mutants of Rab17 delays the transport of HA to the plasma membrane, while overexpression of Rab23 DN reduces HA expression on the cell surface[29]. However, our study demonstrated that silencing Rab17 also slightly downregulated the surface distribution of HA, whereas silencing Rab23 even slightly enhanced the surface distribution of HA. These discrepancies may be due to differences in cell types, with Sato et al.'s study using polarized MDCK cells and ours using A549 cells, which may exhibit distinct expression patterns of Rab GTPase family gene expression profiles. On the other hand, methodological differences may also contribute to the observed discrepancies, as silencing certain genes could trigger compensatory effects from other members of the same gene family. Moreover, studies have shown that Rab6 is essential for anterograde transport from the Golgi apparatus[30,31], and regulates the transport of proteins and cargoes, including VSV G[32] and HSV[33]. Our results also demonstrate that silencing Rab6 leads to a slight reduction in HA protein levels on the cell surface. Therefore, Rab6 and Rab17 may also be involved in the transport of HA protein to the plasma membrane, although its role is much smaller than that of Rab27a.

Our data show that Rab27a exhibits some degree of colocalization with both the ER and the Golgi apparatus (Supplementary Fig. 4b, c, and h), indicating that Rab27a-positive vesicles cannot be definitively classified as Golgi-derived vesicles and may also originate from the ER or the ER–Golgi intermediate compartment (ERGIC). Nevertheless, results from the RUSH system demonstrate that following synchronized release of viral membrane proteins in Rab27a KO and A549-Cas9 cells, the accumulation of these proteins in the Golgi is comparable between the two cell lines, whereas the amount reaching the plasma membrane is reduced in Rab27a knockout cells. These findings suggest that there may be a subset of Rab27a-positive vesicles derived from the Golgi that contribute to viral protein transport. However, the exact nature of the transport vesicles remains to be further elucidated.

Rab27a enhances the replication of various subtypes of IAV by promoting the transport of viral membrane proteins. In fact, multiple studies demonstrated that Rab27a influences the replication of other viruses through different mechanisms. For instance, in a mouse model of *Griscelli* syndrome with Rab27a deletion, the replication of mouse leukemia virus was impaired due to reduced multivesicular body exocytosis, which restricted viral release[34]. Moreover, Rab27a regulates the replication of human cytomegalovirus[35], herpes simplex virus type 1[36] and Seneca Valley virus[37], all of which assemble in the cytoplasm and depend on Rab27a-mediated exocytosis for efficient release. Another mechanism by which Rab27a regulates viral replication involves its role in microRNA transport via exosomes. Hepatitis C virus enhances utilizes Rab27a-dependent delivery of microRNA miR-122 to enhance viral genome abundance and facilitate replication[38]. Conversely, foot-and-mouth disease virus suppresses exosome release by downregulating Rab27a, thereby reducing the secretion of immune-stimulatory microRNA-136. This strategy helps the virus evade innate immune defenses and promotes replication[39]. Although our result suggests that Rab27a KO does not affect the primary transcription and

https://doi.org/10.1038/s41467-025-61587-3

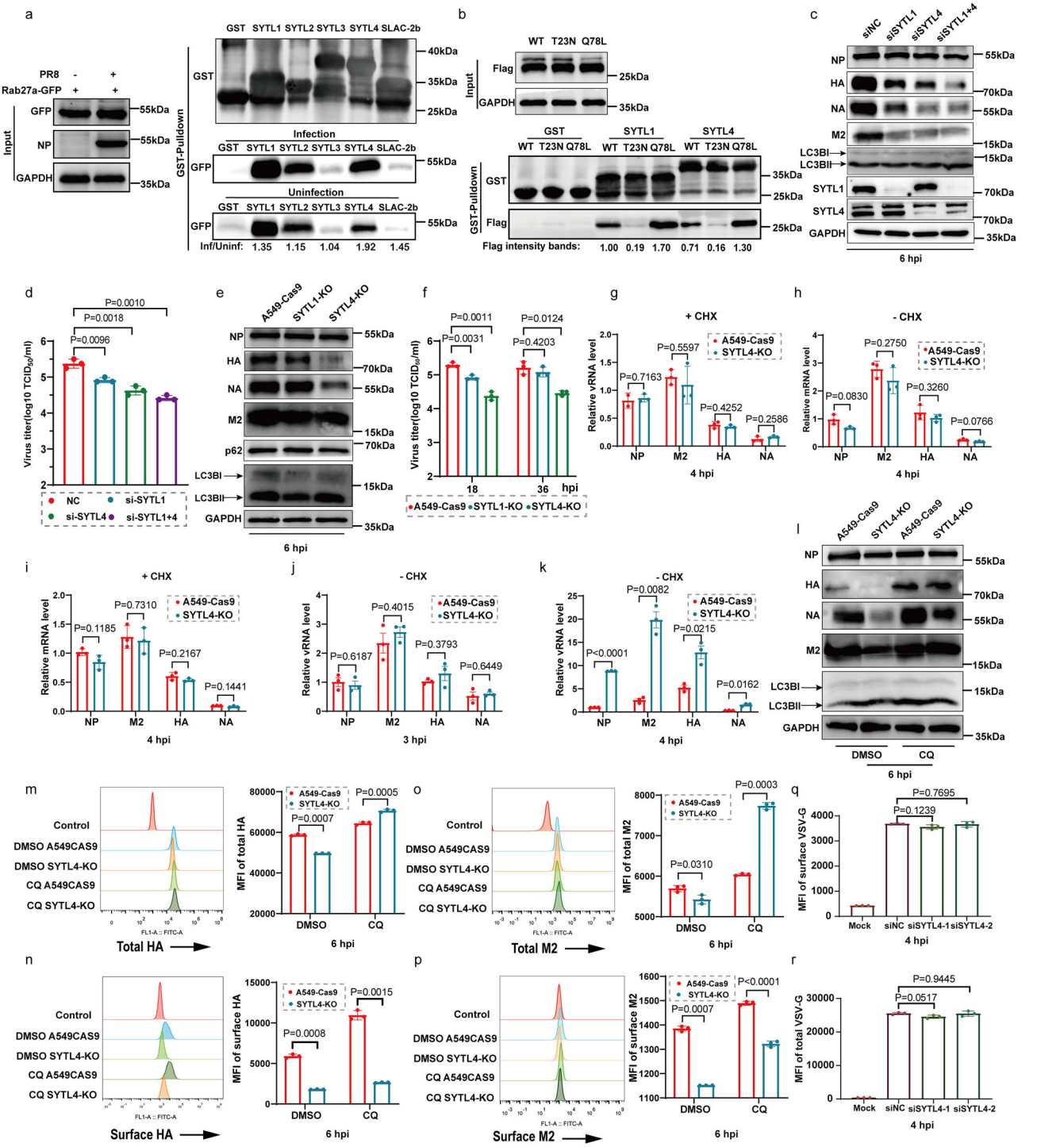

Fig. 6 | SYTL1 and SYTL4 are two Rab27 effectors involved in IAV membrane protein transport. a HEK293T cells were transfected with Rab27a-GFP for 24 h, then infected with HM virus (MOI, 0.1) or left uninfected. At 12 hpi, cell lysates were subjected to GST affinity pull-down assays. **b** HEK293T cells were transfected with Flag-Rab27a WT, Flag-Rab27a-Q78L, and Flag-Rab27a-T23N for 24 h, then cell lysates were used for GST affinity pull-down assays. **c**, **d** A549 cells transfected with siSYTL1/4 or siNC for 24 h were infected with HM virus. Protein levels were detected at 6 hpi (**c**) (MOI, 10), and viral titers of supernatants were determined by $TCID_{50}$ assay at 24 hpi (**d**) (MOI, 0.1). **e**, **f** SYTL1/4-KO and A549-Cas9 cells were infected with HM virus. Protein levels were detected at 6 hpi (**e**) (MOI, 10), and viral titers of supernatants were determined by $TCID_{50}$ assay at 18 and 36 hpi (**f**) (MOI, 0.1). **g**–**k** SYTL4-KO and A549-Cas9 cells were pretreated with CHX (100 μM) or DMSO for 4 h, then infected with HM virus (MOI, 10) and treated with CHX (350 μM) or DMSO. mRNA and vRNA levels of viral genes were detected by qRT-PCR. **l** SYTL4-KO and A549-Cas9 were pretreated with CQ (12.5 μM) or DMSO for 6 h, then cells infected with HM virus (MOI, 10) and treated with CQ (25 μM) for 6 h. **m**–**p** SYTL4-KO and A549-Cas9 cells were pretreated with CQ (12.5 μM) or DMSO for 6 h, then infected with HM virus (MOI, 10) and treated with CQ (25 μM). At 6 hpi, both total (**m**, **o**) and cell surface (**n**, **p**) viral membrane proteins levels were measured by flow cytometry. **q**, **r** A549 cells transfected with siSYTL4-1, siSYTL4-2, or siNC for 24 h were infected with VSV-GFP (MOI, 10). Cell surface (**q**) and total (**r**) levels of VSV-G protein were quantified by flow cytometry. Data are presented as mean ± SD from three independent experiments. Statistical significance was determined using a two-tailed Student's *t*-test. Levels of indicated proteins, assessed by western blot in (**a**–**c**, **e**, and **l**), GAPDH served as a loading control.

https://doi.org/10.1038/s41467-025-61587-3

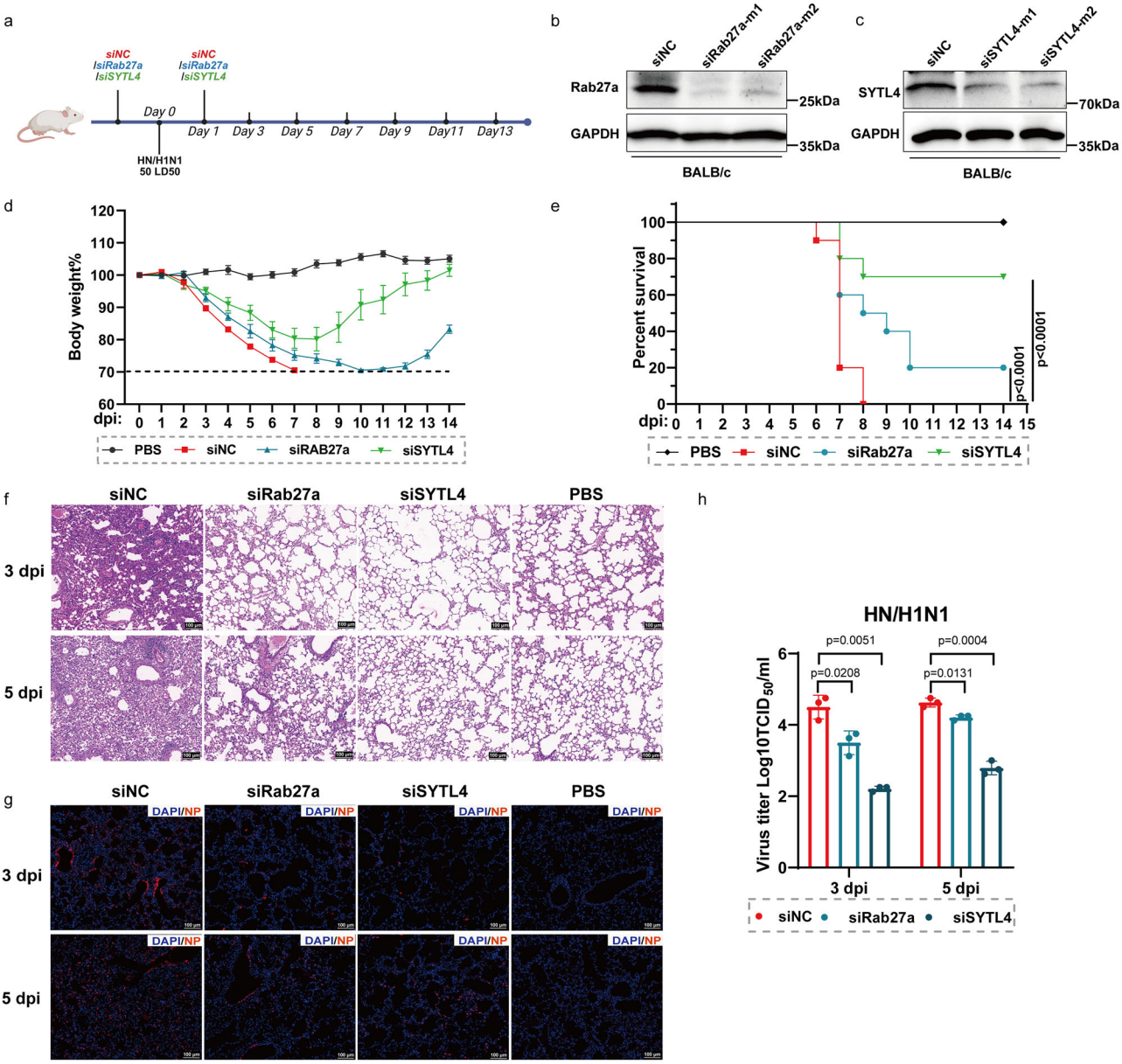

Fig. 7 | SYTL4 is a potential anti-influenza virus drug target. a A flowchart of siRNA treatment and HN/H1N1 infection in a mouse experimental model. Image was created in BioRender. Tong, C. (2025) https://BioRender.com/hq3p0b8. **b**, **c** Western blot analysis of Rab27a expression in siRab27a (**b**), siSYTL4 (**c**) and siNC treated mice at 3 dpi, GAPDH served as a loading control. **d** Body weight changes of PBS and HN/H1N1 infection with siRNAs treatment in mice ($n = 10$). Mice with body weight below 70% of initial were euthanized according to the ethical principles of animal welfare. **e** Survival rates of PBS and HN/H1N1-infected mice with siRNAs treatment ($n = 10$). Survival curves were analyzed using the log-rank test (Mantel-Cox). **f** Pathological lesions in the lungs of mice infected with the indicated virus at 3 and 5 dpi with hematoxylin and eosin (H&E) staining. Scale bars, 100 μm. **g** Immunofluorescent staining of lung sections from mice infected with the indicated virus at 3 and 5 dpi. Viral NP antigen was stained red, and the cell nucleus was stained blue. Scale bars, 100 μm. **h** Virus titers in the lungs of infected mice ($n = 3$) at 3 and 5 dpi. The data shown in (**d** and **h**) are means ± SD ($n = 10$ for (**c**) and $n = 3$ for (**h**) biologically independent experiments). Statistical significance was analyzed using a two-tailed Student's *t*-test.

replication of the viral genome in a single round replication (Fig. 2b, c), it remains unclear whether viral genome abundance is disrupted via the exosome pathway following Rab27a silencing.

Our results demonstrate that Rab27a KO leads to higher levels of viral membrane proteins compared to the A549-Cas9 cells at 6 hpi, while SYTL1 and SYTL4 KO reduce viral membrane protein levels. These differences can be attributed to variations in autophagy levels among these cells. Notably, knocking out these genes had a much smaller impact on NP protein levels compared to membrane proteins. This is likely because viral membrane proteins attach to vesicles, and when transport is blocked, they are likely to follow the movement of the cytoskeleton, making them easily degraded by lysosomes. In contrast, vRNPs are transported via tubular membrane network of ER to the bottom of the cell surface, where they wrapped in Rab11 positive vesicles waiting to be assembled, making them less susceptible to degradation[6,40].

We found that Rab27a KO led to reduced autophagy level, which in turn caused M2 accumulation and elevated its levels at the plasma membrane. Subsequent results showed that overexpression of Rab27a promoted the distribution of M2 on the cell surface. Importantly, using the RUSH system, M2 was simultaneously released from Golgi apparatus of Rab27a KO and A549-Cas9 cells, with lower levels of M2

reaching the surface in Rab27a KO cells, indicating that Rab27a regulates the transport of M2 to cell surface. Recent studies have demonstrated that the LIR motif of M2 is critical for its localization to the plasma membrane, which promoting its trafficking to cell surface through interaction with LC3[41]. This suggests that M2 can indeed bypass the ER-Golgi apparatus pathway and be transported directly to the plasma membrane via the secretory autophagy pathway. Although Rab27a knockout partially reduces LC3 levels, we propose that the remaining LC3 may still be sufficient to support the transport of accumulated M2 to the cell surface in Rab27a KO cells. In addition, the trafficking of secretory autophagosomes to the plasma membrane is regulated by host factors such as Rab8a[42], Rab37[43], STX3/4[44], and SNAP23/39[44], among others, which may also influence the transport of M2 to the plasma membrane. However, the underlying mechanisms remain to be elucidated. Therefore, we speculate that M2 reaches the plasma membrane via two distinct pathways: a Rab27a-dependent ER-Golgi transport pathway and a Rab27a-independent autophagosome-mediated transport pathway.

A total of 12 Rab27 effectors have been identified in humans[45], each exhibiting selective expression in specific cell types. In this study, qPCR analysis revealed that 10 of these effectors are expressed in A549 cells (Supplementary Fig. 5a). Subsequently, we investigated potential functional effectors using GST-pulldown assays and observed that SYTL4 and SYTL1 consistently demonstrated stable interactions with Rab27a in the infection group across multiple repeated experiments (Fig. 6a). Although the interaction between SLAC-2b and Rab27a was upregulated following viral infection, this interaction proved to be weak and unstable in subsequent repeated experiments. Therefore, our validation efforts focused on the roles of SYTL4 and SYTL1 in IAV infection. Interestingly, while both knockout and knockdown of Rab27a and SYTL4 significantly inhibited IAV replication in vitro, the protection conferred by SYTL4 knockdown in mouse infection model was markedly higher than that of Rab27a knockdown (Fig. 7d, e). This discrepancy may stem from partial compensatory functionality of Rab27b in the absence of Rab27a. In summary, our findings suggest that SYTL4 represents a promising drug target with significant therapeutic potential.

In conclusion, this study revealed the molecular mechanism by which Rab27a and its effectors facilitate the transport of influenza virus membrane proteins, filling a crucial gap in IAV life cycle mechanism research and providing a potential host target for the antiviral drugs development.

Methods

Ethics statement

All animal experiments in this study were performed in strict accordance with the Guide for the Care and Use of Laboratory Animals issued by the Ministry of Science and Technology of the People's Republic of China. The experimental protocols were reviewed and approved by the Hubei Administrative Committee for Laboratory Animals (Approval No: HZAUMO-2023-0245).

Experimental model and subject details

Cells. A549 cells were cultured in HAM'S/F-12 medium (HyClone, SH30026.01); HEK293T cells were cultured in RPMI 1640 medium (HyClone, SH30809.01); and MDCK and BHK cells were cultured in DMEM/high glucose medium (HyClone, SH30022.01). All media were supplemented with 10% heat-inactivated fetal bovine serum (FBS; PAN Biotech, P30-3302). Cells were maintained in a 37 °C humidified incubator with 5% CO_2.

Viruses. The H5N1 strain A/duck/Hubei/Hangmei01/2006 (HM)[46], H9N2 strain A/chicken/Shanghai/SC1972013 (SH13), and H1N1 strain A/Puerto Rico/8/1934 (PR8) viruses were stored in our laboratory. The recombinant VSV-GFP was generously provided by Professor Shengbo Cao (Hubei, China). The GFP gene was from plasmid pIRES2-eGFP (Clontech, PaloAlto, CA, USA) and was inserted between genes of VSV glycoprotein and Matrix protein. Viral titers were determined by 50% tissue culture infectious dose ($TCID_{50}$) method on MDCK cells for IAV or A549 cells for VSV-GFP. A549 cells were infected with HM virus or VSV-GFP at multiplicity of infection (MOI) of 0.1 or 10. After 1 h adsorption, cells were washed once with warm phosphate-buffered saline (PBS (pH 7.2), HyClone, SH30256.01) and then incubated in HAM'S/F-12 at 37 °C. For infections with other viruses, the final maintenance medium was replaced with serum free HAM'S/F-12 supplemented with N-tosyl-L-phenylalanine chloromethyl ketone (TPCK) trypsin (0.25 μg/ml). Then, virus stocks were collected at 12, 24, 36, or 48 hpi, serially diluted in DMEM, and adsorbed onto confluent MDCK cells for 1 h at 37 °C. Subsequently, the inoculum was removed, cells were washed twice with PBS, and cultured with serum-free DMEM for HM virus and VSV-GFP or DMEM containing TPCK trypsin (0.25 μg/ml) for other viruses at 37 °C. After 3d of incubation, virus titers were calculated as $\log_{10}TCID_{50}$/ml on MDCK or A549 cells, using the Reed and Muench method. All experiments involving HM virus were performed in the Biosafety Level 3 laboratory at Huazhong Agricultural University.

Mice. The 4 to 6 weeks old female BALB/c mice were purchased from Laboratory Animal Center of Huazhong Agricultural University. Mice were housed in a pathogen-free barrier facility with a 12-h light/dark cycle and provided ad libitum access to a standard chow diet and water. All mice used in this study were in good health and had not been subjected to any prior experimental procedures.

Antibodies and reagents

The antibodies used in this study and their sources are as follows:

Rabbit polyclonal antibodies: Rab37, Rab3b, Rab6a, Rab11a, Rab17, Rab23, Rab25, Rab27a, Rab27b, SYTL4, SQSTM1, ATB4B, TNG46, GM130 (Proteintech; 13051-1-AP, 15774-1-AP, 10187-2-AP, 20229-1-AP, 17501-1-AP, 11101-1-AP, 13189-1-AP, 16868-1-AP, 13412-1-AP, 12128-1-AP, 18420-1-AP, 15131-1-AP, 13573-1-AP, 11308-1-AP), Rab38 (Abways, AY3825), SYTL1 (Bethyl, A305-648A-T), BECN1 (ABclonal Biotechnology, A7353), Phospho-ATG4B (Ser316) (Affinity Biosciences, AF3505), ATG16L1 (HUABIO, ET7106-65), and IAV M2, NP, NS1, and HA (GeneTex; GTX125951, GTX30852, GTX125990, GTX127357). Rabbit monoclonal antibodies: ATG7 (Cell Signaling Technology, 8558S) and MAP1LC3B/LC3B (Novus Biologicals, NB100-2220). Mouse monoclonal antibodies: HA-tag (MBL, M180-3), Flag-tag, Calnexin (Proteintech, 66008-4-Ig, 66903-1-Ig), GAPDH (California Bioscience, CB100127), GFP-tag (CWBIO, CW0258A), ATG5 (Arigo Biolaboratories, ARG54822), GST-tag (HUABIO, EM80701), and VSV-G (Abbkine, ABT2180).

Secondary antibodies: FITC-conjugated goat anti-mouse and anti-rabbit antibodies (Sungene Biotech; GM200G-02C, GR200G-02C). 594-conjugated goat anti-mouse and anti-rabbit antibodies (Sungene Biotech; GM200G-43C, GR200G-43C). 647-conjugated goat anti-rabbit IgG (ABclonal Biotechnology, AS060). HRP-conjugated anti-mouse and anti-rabbit antibodies (Beijing Biodragon Immunotechnologies; BF03001, BF03008).

Reagents: Cycloheximide (CHX) (Sigma-Aldrich, 66819), Bafilomycin A1 (BafA1) (Selleck, S1413), Chloroquine (CQ) (Selleck, S6999), Oseltamivir (Selleck, S2597), and MG132 (Selleck, S2619).

Plasmids and siRNA oligonucleotides

Full-length cDNA encoding HM virus NA, HA, M2, NP, Rab27a, and ATG4B were amplified by RT-PCR from total RNA extracted from A549 cells infected with HM virus using specific primers (available upon request). These cDNA sequences were cloned into the p3 × Flag-CMV (Rab27a-Flag, ATG4B-Flag), HA-pCAGGS (HA-Rab27a, HA-ATG4B), pEGFP-N1 (Rab27a-EGFP), pLenti6.4-CMV (pLenti6.4-GFP-Rab27a), and pcDNA 3.4 (HA-Flag, M2-Flag, NP-Flag, NA-Flag, and Flag-Rab27a). The

SHD domain sequences of SYTL1, SYTL2, SYTL3, SYTL4, and Slac-2b were synthesized by Beijing Tsingke Biotech and cloned into pGEX-4T-1. Rab27a mutant sequences (Q78L and T23N) were generated using site-directed mutagenesis primers, amplified from Rab27a (WT)-Flag, and cloned into p3 × Flag-CMV (Rab27a Q78L-Flag, Rab27a T23N-Flag). Synonymous mutations of these mutants to avoid sgRNA recognition were cloned into pLenti6.4-CMV (pLenti6.4-Flag-Rab27a WT, pLenti6.4-Flag-Rab27a T23N, pLenti6.4-Flag-Rab27a Q78L). For the RUSH system, the reporter gene was replaced with influenza virus HA/M2 or VSV G according to the ref. 21, and the sequence was segmented and synthesized by Beijing Qingke Biotechnology Company and cloned into pLV2-CMV-IRES-GFP vector, including pLV2-Str-HA (Tag) -Li-ISRE-HA-SBP-GFP, pLV2-Str-HA (Tag) -Li-ISRE-VSV G-SBP-GFP, Str-HA (Tag) -Golgin-84-ISRE-M2-SBP-GFP.

The following empty vectors were stored in our laboratory: p3 × Flag-CMV, HA-pCAGGS, pEGFP-N1, pcDNA 3.4, pGEX-4T-1, pLenti6.4-CMV, PMD2.G, pLV2-CMV-IRES-GFP, psPAX2. Lenti-CRISPR-sgRNA-Puro and Lenti-CRISPR-sgRNA-GFP were donated by Professor Shengsong Xie (Hubei, China).

Sequences of siRNAs used in this study are listed in Supplementary Data 1.

Generation and validation of gene knockout and stable expression cell lines

Rab27a-, Rab27b-, SYTL1- and SYTL4- KO A549 cells were generated by using the CRISPR/Cas9 system as described previously[47,48]. Single guide RNA (sgRNA) sequences targeting Rab27a (5′-CCGGATGGAGCCACTGGCAG-3′), Rab27b (5′-CCTGGCCCTCGGGGATTCAG-3′), SYTL1 (5′-TGCGATGGGTGGCCCCTCTG-3′), and SYTL4 (5′-AAAAGGAAAGGGGCCAAGAG-3′) were cloned into Lenti-CRISPR-sgRNA-Puro or Lenti-CRISPR-sgRNA-GFP vectors. Lentiviruses were generated by co-transfecting HEK293T cells with above plasmids, the packaging plasmid psPAX2, and the membrane plasmid pMD2.G using Lipofectamine™ 2000. Lentiviral supernatants were collected 72 h post-transfection, filtered (0.45 μm), and stored at −80 °C. A549-Cas9 cells were infected with lentiviruses carrying Rab27a, SYTL1, or SYTL4 sgRNAs in the presence of 8 μg/ml polybrene, and positive clones were selected with puromycin (2.5 μg/ml) for 48–60 hpi. Rab27b sgRNA lentivirus-infected cells were screened based on GFP fluorescence. Rab27a and Rab27b double-knockout cells were generated by infecting Rab27a KO monoclonal cells with Rab27b lentivirus, followed by GFP-based selection. Monoclonal cells were isolated using the limiting dilution method in 96-well plates, expanded, and verified via western blotting and sequencing.

Polyclonal stable A549 cell lines expressing Flag-Rab27a wild-type (WT)/T23N/ Q78L mutants in Rab27a-KO cells or monoclonal GFP-Rab27a in wild-type A549 cells were established via lentiviral transduction. Lentiviruses were generated by co-transfecting HEK293T cells with plasmids (e.g., pLenti6.4-Flag-Rab27a WT/T23N/Q78L, or pLenti6.4-GFP-Rab27a), the packaging plasmid psPAX2, and the membrane plasmid pMD2.G using Lipofectamine™ 2000. Lentiviral supernatants were collected 72 h post-transfection, filtered (0.45 μm), and stored at −80 °C. Rab27a-KO A549 cells were infected with lentiviruses containing Flag-Rab27a constructs in the presence of 8 μg/ml polybrene, while wild-type A549 cells were infected with GFP-Rab27a lentivirus under similar conditions. Stable expression of Rab27a constructs was confirmed via western blotting, with GAPDH as the loading control, and GFP fluorescence was visualized using a fluorescence microscope.

RNA isolation and qRT-PCR

Total RNA was extracted from cells using TRIzol reagent (Invitrogen, USA) following the manufacturer's protocol. One to two micrograms of RNA were used for cDNA synthesis with reverse transcriptase (ABclonal, RK20433). qRT-PCR was performed on a ViiA7 Real-Time PCR System (Applied Biosystems, USA) using FastStart Universal SYBR Green Master Mix (ABclonal, RK21203). The PCR conditions were: 50 °C for 2 min, 95 °C for 10 min, followed by 40 cycles of 95 °C for 15 s and 60 °C for 30 s.

To ensure the specific detection of viral RNA (vRNA) and messenger RNA (mRNA) of IAV, primers for reverse transcription included an 18- to 20-nucleotide tag unrelated to the influenza virus at the 5′ end. Tagged cDNA was subsequently amplified by qRT-PCR using the tag sequence as the forward primer and a segment-specific reverse primer. Expression levels of cellular mRNA and intracellular viral RNA were normalized to 18S rRNA. Primer sequences used for qRT-PCR are provided in Supplementary Data 2.

Cell viability assay

Cell proliferation after gene silencing or knockout was assessed using the CCK-8 assay (GLPBIO, GK10001) according to the manufacturer's protocol. For silencing experiments, cells seeded in 96-well plates were transfected with si-Rab27a, si-SYTL4, si-SYTL1, or si-NC, and cell viability was measured 24 h post-transfection. For knockout cell lines, equal numbers of knockout cells and A549-Cas9 control cells were seeded in 96-well plates at ~50% confluence, and cell viability was measured at 12, 24, and 36 h. At each time point, CCK-8 reagent was added to the wells, and absorbance at 450 nm was recorded using a microplate reader after 1 h incubation.

Western blot

Cells were lysed in cell lysis buffer for western blotting and IP (Beyotime, P0013) or mammalian cell lysis buffer (CWBIO, CW0889) supplemented with protease inhibitors (Roche, 04693132001). Lysates were clarified by centrifugation, and equal amounts of protein were separated by SDS-PAGE and transferred onto nitrocellulose membranes (GE Healthcare Life Sciences, 10600001 and 10600002). Membranes were blocked with 5% bovine serum albumin (BSA; Sigma, A1933) in tris-buffered saline with Tween (TBST; Sigma, SRE0031) and incubated with primary antibodies, followed by HRP-conjugated secondary antibodies. Protein bands were visualized using the WesternBright™ ECL detection kit (Advansta, K-12045-D50) and an ECL detection system (Amersham Biosciences, NJ, USA). All bands were detected within the linear range of the system.

Flow cytometry analysis

Flow cytometry analysis was performed as previously described[49]. Briefly, cells were digested and resuspended in complete growth medium. For total protein detection, cells were fixed with 4% paraformaldehyde for 10 min at room temperature, followed by permeabilization with 0.2% Triton X-100 for 5 min. For surface protein detection, cells were incubated on ice with PBS containing 5% FBS for 1 h. Subsequently, cells were incubated with primary antibodies on ice for 1 h, followed by staining with fluorescent secondary antibodies for 40 min on ice. To distinguish live and dead cells during surface protein analysis, Propidium Iodide (PI) staining was performed at 37 °C for 30 min. After each step, cells were washed three times with PBS: live cells at 1500 rpm for 3 min, and dead cells at 4000 rpm for 3 min. Samples were analyzed using a BD FACSCanto II Flow Cytometer, and data were processed with FlowJo v10 software.

GST pulldown

Glutathione S-transferase (GST)-fused SHD domains of SYTL1, SYTL2, SYTL3, SYTL4, and Slac-2b, as well as GST alone, were expressed in *Escherichia coli* and purified using glutathione-Sepharose beads (Solarbio). The purity of the GST and GST-SHD proteins was confirmed by Coomassie blue staining. HEK293T cells cultured in 10 cm dishes were transfected with

15 μg of Rab27a-Flag plasmid. At 24 h post-transfection, cells were infected with or without PR8 virus (MOI, 0.01). After 24 hpi, cells were lysed in 800 μl of lysis buffer for western blotting and IP. Purified GST and GST-SHD proteins (SYTL1, SYTL2, SYTL3, SYTL4, and Slac-2b) were incubated with 40 μl of glutathione-Sepharose beads at 4 °C for 3 h with gentle rocking. After five washes with lysis buffer, HEK293T cell lysates were added to the beads and incubated overnight at 4 °C. The beads were then washed five more times, and bound proteins were analyzed by western blotting.

Immunofluorescence and confocal microscopy

A549 or HEK293T cells were plated on coverslips in confocal dishes and infected with HM virus or transfected with the indicated plasmids. At the specified time points post-infection or transfection, cells were fixed with 4% paraformaldehyde for 15 min, permeabilized with 0.2% Triton X-100 (Sigma-Aldrich, X100) in PBS for 10 min, and blocked with 4% BSA at room temperature for 1 h. Cells were then incubated with the corresponding primary antibodies at 4 °C overnight, followed by Alexa Fluor FITC-, 647-, or 594-conjugated goat anti-mouse or anti-rabbit secondary antibodies for 1 h at room temperature. Nuclei were stained with DAPI (Invitrogen, 00–4959-52) for 10 min. After each step, cells were washed five times with PBS. Confocal images were acquired using a Carl Zeiss LSM 880 confocal microscope, and data were analyzed using ZEN 2.3 LITE software. ImageJ and Fiji were used for statistical analysis of the images.

Transmission electron microscope

Cells were seeded in 100 mm dishes and infected with HM virus (MOI = 10). At the specified time points post-infection, cells were fixed with cold 2.5% ultra-pure glutaraldehyde and harvested using a cell scraper. Representative ultrastructural images were obtained using a transmission electron microscope (FEI, Tecnai G2 20 TWIN, 120 kV).

Computer modeling of protein binding

The crystal structure of human ATG4B-LC3 (1-120) complex (PDB ID: 2z0d) and Rab27a (PDB ID: 6huf) were obtained from the RCSB PDB database (https://www.rcsb.org/). Potential interaction between Rab27a or ATG4B and LC3 were predicted using the GRAMM protein docking and molecular superposition program (https://gramm.compbio.ku.edu/gramm). Structural models and docking results were visualized and analyzed using PyMOL (https://pymol.org/2/).

RUSH (retention using selective hooks) assays

RUSH assays were performed in A549-Cas9 and Rab27a knockout cells to study intracellular cargo transport. Cells were seeded on coverslips placed in confocal dishes and allowed to adhere. The cells were then transfected with one of the following plasmids: pLV2-Str-HA (Tag) -Li-ISRE-HA-SBP-GFP, pLV2-Str-HA (Tag) -Li-ISRE-VSV G-SBP-GFP, or pLV2-Str-HA (Tag) -Golgin-84-ISRE-M2-SBP-GFP, for 24 h. To activate the RUSH system, D-biotin (400 μM; Sigma, B4639) was added to each well to release cargo proteins anchored on the endoplasmic reticulum (ER) or Golgi apparatus. Cells were then fixed and stained at designated time points, and cargo transport was visualized via confocal microscopy using indirect immunofluorescence assays. The co-localization of cargo proteins with different organelles or proportion of cargo proteins on the cell surface was analyzed using Fiji software.

In vivo studies

5 nmol Cholesterol-conjugated and 2′-OME-modified siRNAs targeting mouse Rab27a (siRab27a), mouse SYTL4 (siSYTL4), or a negative control (siNC) were nasally administered to 4–6-week-old female BALB/c SPF mice. Two days later, mice from each group were anesthetized, sacrificed, and lung tissues were homogenized for western blot analysis to assess Rab27a and SYTL4 expression. For infection studies, mice were nasally instilled with 5 nmol of siRab27a, siSYTL4, or siNC at 1 day prior to infection and again at 1 dpi. Mice were challenged with 50 LD_{50} of HN/H1N1 virus or an equivalent volume of PBS ($n = 10$ per group). Body weight loss and survival rates were monitored daily for 14 days. Mice that lost ≥30% of their initial body weight were humanely euthanized. To evaluate viral replication and lung lesions, an additional 6 mice per group were treated following the same procedure. At 3 and 5 dpi, mice were euthanized, and lung tissues were collected for further analysis.

Quantification and statistical analysis

Data were analyzed using GraphPad Prism software and are expressed as means ± standard deviations (SD). Statistical analysis was performed by a paired two-tailed Student's *t*-test. ns, $p > 0.05$, not significant; $p \le 0.05$, significant; $p \le 0.01$, very significant; $p \le 0.001$, highly significant; $p \le 0.0001$, extremely significant.

Reporting summary

Further information on research design is available in the Nature Portfolio Reporting Summary linked to this article.

Data availability

All data supporting the findings of the study are available within the main text, the Supplementary Information and the Source Data files are provided with this paper. Source data are provided with this paper.

References

1. Iuliano, A. D. et al. Estimates of global seasonal influenza-associated respiratory mortality: a modelling study. *Lancet* **391**, 1285–1300 (2018).
2. Rossman, J. S. & Lamb, R. A. Influenza virus assembly and budding. *Virology* **411**, 229–236 (2011).
3. Eisfeld, A. J., Kawakami, E., Watanabe, T., Neumann, G. & Kawaoka, Y. RAB11A Is Essential for transport of the influenza virus genome to the plasma membrane. *J. Virol.* **85**, 6117–6126 (2011).
4. Amorim, M. J. et al. A Rab11-and microtubule-dependent mechanism for cytoplasmic transport of influenza A virus viral RNA. *J. Virol.* **85**, 4143–4156 (2011).
5. Avilov, S. V., Moisy, D., Naffakh, N. & Cusack, S. Influenza A virus progeny vRNP trafficking in live infected cells studied with the virus-encoded fluorescently tagged PB2 protein. *Vaccine* **30**, 7411–7417 (2012).
6. Alenquer, M. et al. Influenza A virus ribonucleoproteins form liquid organelles at endoplasmic reticulum exit sites. *Nat. Commun.* **10**, 1629 (2019).
7. De Matteis, M. A. & Luini, A. Exiting the Golgi complex. *Nat. Rev. Mol. Cell Biol.* **9**, 273–284 (2008).
8. Stenmark, H. Rab GTPases as coordinators of vesicle traffic. *Nat. Rev. Mol. Cell Biol.***10**, 513–525 (2009).
9. Zhen, Y. & Stenmark, H. Cellular functions of Rab GTPases at a glance. *J. Cell Sci.* **128**, 3171–3176 (2015).
10. Ostrowski, M. et al. Rab27a and Rab27b control different steps of the exosome secretion pathway. *Nat. Cell Biol.* **12**, 19–30 (2010).
11. Yi, C. et al. Genome-wide CRISPR-Cas9 screening identifies the CYTH2 host gene as a potential therapeutic target of influenza viral infection. *Cell Rep.* **38**, 110559 (2022).
12. Luo, M. Influenza virus entry. *Adv. Exp. Med. Biol.* **726**, 201–221 (2012).
13. Eisfeld, A. J., Neumann, G. & Kawaoka, Y. At the centre: influenza A virus ribonucleoproteins. *Nat. Rev. Microbiol.* **13**, 28–41 (2015).
14. Nayak, D. P., Balogun, R. A., Yamada, H., Zhou, Z. H. & Barman, S. Influenza virus morphogenesis and budding. *Virus Res.* **143**, 147–161 (2009).

15. Yang, C. et al. The nucleolar protein LYAR facilitates ribonucleoprotein assembly of influenza A virus. *J. Virol.* **92**, https://doi.org/10.1128/JVI.01042-18 (2018).
16. Rindler, M. J., Ivanov, I. E., Plesken, H., Rodriguez-Boulan, E. & Sabatini, D. D. Viral glycoproteins destined for apical or basolateral plasma membrane domains traverse the same Golgi apparatus during their intracellular transport in doubly infected Madin-Darby canine kidney cells. *J. Cell Biol.* **98**, 1304–1319 (1984).
17. Rindler, M. J., Ivanov, I. E., Plesken, H. & Sabatini, D. D. Polarized delivery of viral glycoproteins to the apical and basolateral plasma membranes of Madin-Darby canine kidney cells infected with temperature-sensitive viruses. *J. Cell Biol.* **100**, 136–151 (1985).
18. Martin-Sancho, L. et al. Restriction factor compendium for influenza A virus reveals a mechanism for evasion of autophagy. *Nat. Microbiol.* **6**, 1319–1333 (2021).
19. Beale, R. et al. A LC3-interacting motif in the influenza A virus M2 protein is required to subvert autophagy and maintain virion stability. *Cell Host Microbe* **15**, 239–247 (2014).
20. Pengo, N., Agrotis, A., Prak, K., Jones, J. & Ketteler, R. A reversible phospho-switch mediated by ULK1 regulates the activity of autophagy protease ATG4B. *Nat. Commun.* **8**, 294 (2017).
21. Boncompain, G. et al. Synchronization of secretory protein traffic in populations of cells. *Nat. Methods* **9**, 493–498 (2012).
22. McKimm-Breschkin, J. L. Influenza neuraminidase inhibitors: antiviral action and mechanisms of resistance. *Influenza Other Respir. Viruses* **7**, 1201–1208 (2013).
23. Ohuchi, M., Asaoka, N., Sakai, T. & Ohuchi, R. Roles of neuraminidase in the initial stage of influenza virus infection. *Microbes Infect.* **8**, 1287–1293 (2006).
24. Matrosovich, M. N., Matrosovich, T. Y., Gray, T., Roberts, N. A. & Klenk, H. D. Neuraminidase is important for the initiation of influenza virus infection in human airway epithelium. *J. Virol.* **78**, 12665–12667 (2004).
25. Catz, S. D. Regulation of vesicular trafficking and leukocyte function by Rab27 GTPases and their effectors. *J. Leukoc. Biol.* **94**, 613–622 (2013).
26. Yang, M. Q. et al. Interferon regulatory factor 1-Rab27a regulated extracellular vesicles promote liver ischemia/reperfusion injury. *Hepatology* **67**, 1056–1070 (2018).
27. Huber, L. A. et al. Rab8, a small GTPase involved in vesicular traffic between the TGN and the basolateral plasma membrane. *J. Cell Biol.* **123**, 35–45 (1993).
28. Zhuang, R. et al. Rab26 restricts insulin secretion via sequestering Synaptotagmin-1. *PLoS Biol.* **21**, e3002142 (2023).
29. Sato, R. et al. Apical trafficking pathways of influenza A virus HA and NA via Rab17- and Rab23-positive compartments. *Front. Microbiol.* **10**, 1857 (2019).
30. Miserey-Lenkei, S. et al. Coupling fission and exit of RAB6 vesicles at Golgi hotspots through kinesin-myosin interactions. *Nat. Commun.* **8**, 1254 (2017).
31. Fourriere, L. et al. RAB6 and microtubules restrict protein secretion to focal adhesions. *J. Cell Biol.* **218**, 2215–2231 (2019).
32. Dickson, L. J., Liu, S. & Storrie, B. Rab6 is required for rapid, cisternal-specific, intra-Golgi cargo transport. *Sci. Rep.* **10**, 16604 (2020).
33. Bergeman, M. H., Velarde, K., Hargis, H. L., Glenn, H. L. & Hogue, I. B. The Rab6 post-Golgi secretory pathway contributes to herpes simplex virus 1 (HSV-1) egress. *J. Virol.* **98**, e0059924 (2024).
34. Chan, W. T. et al. Murine leukemia virus spreading in mice impaired in the biogenesis of secretory lysosomes and Ca2 + -regulated exocytosis. *PLoS ONE* **3**, e2713 (2008).
35. Fraile-Ramos, A., Cepeda, V., Elstak, E. & van der Sluijs, P. Rab27a is required for human cytomegalovirus assembly. *PLoS ONE* **5**, e15318 (2010).
36. Bello-Morales, R. et al. Role of the small GTPase Rab27a during herpes simplex virus infection of oligodendrocytic cells. *BMC Microbiol.* **12**, 265 (2012).
37. Xu, G. et al. Intercellular transmission of Seneca Valley virus mediated by exosomes. *Vet. Res.* **51**, 91 (2020).
38. Chen, T. C., Hsieh, C. H. & Sarnow, P. Supporting role for GTPase Rab27a in hepatitis C virus RNA replication through a novel miR-122-mediated effect. *PLoS Pathog.* **11**, e1005116 (2015).
39. Xu, G. et al. Foot-and-mouth disease virus degrades Rab27a to suppress the exosome-mediated antiviral immune response. *Vet. Microbiol.* **251**, 108889 (2020).
40. de Castro Martin, I. F. et al. Influenza virus genome reaches the plasma membrane via a modified endoplasmic reticulum and Rab11-dependent vesicles. *Nat. Commun.* **8**, 1396 (2017).
41. Figueras-Novoa, C. et al. Caspase cleavage of influenza A virus M2 disrupts M2-LC3 interaction and regulates virion production. *EMBO Rep.* **26**, 1768–1791 (2025).
42. Dupont, N. et al. Autophagy-based unconventional secretory pathway for extracellular delivery of IL-1β. *Embo J.* **30**, 4701–4711 (2011).
43. Wu, S. Y. et al. Secretory autophagy-promoted cargo exocytosis requires active RAB37. *Autophagy* **20**, 933–934 (2024).
44. Kimura, T. et al. Dedicated SNAREs and specialized TRIM cargo receptors mediate secretory autophagy. *Embo J.* **36**, 42–60 (2017).
45. Izumi, T. In vivo roles of Rab27 and its effectors in exocytosis. *Cell Struct. Funct.* **46**, 79–94 (2021).
46. Zou, W., Yu, Z., Zhou, H., Tu, J. & Jin, M. Genetic characterization of an H5N1 avian influenza virus with neurovirulence in ducks. *Virus Genes* **38**, 263–268 (2009).
47. Sanjana, N. E., Shalem, O. & Zhang, F. Improved vectors and genome-wide libraries for CRISPR screening. *Nat. Methods* **11**, 783–784 (2014).
48. Xia, Z. et al. Inducible TAP1 negatively regulates the antiviral innate immune response by targeting the TAK1 complex. *J. Immunol.* **198**, 3690–3704 (2017).
49. Liu, X. et al. MARCH8 inhibits influenza A virus infection by targeting viral M2 protein for ubiquitination-dependent degradation in lysosomes. *Nat. Commun.* **12**, 4427 (2021).

Acknowledgements

We acknowledge the support of the National Key Laboratory of Agricultural Microbiology Core Facility for their aid in confocal microscopy and flow cytometry. We also thank Jing Xu, Yeting Wu, and Yingying Xu from public instrument center of the college of Animal Science & Technology and College of Veterinary Medicine of Huazhong Agricultural University for their invaluable support and assistance with various experimental procedures. Figures 5d and 7a were created with Biorender.com, with permission. This work was supported by the National Key Research and Development Program (2021YFD1800204 to H.Z.), the National Natural Science Foundation of China (32025036 & 32430104 to H.Z.), the Fundamental Research Fund for the Central Universities (2662025DKPY009 to H.Z.), Hubei Hongshan Laboratory (2022hszd005 to H.Z.), the earmarked fund for CARS-41 to H.Z.

Author contributions

Conceptualization, H.Zhou and T.Chen; methodology, T.Chen, A.Ouyang, Y.Feng, C.Wu, M.Jiang, J.Zou, S.Tu, L.Ding, Y.Cheng, W.Hu, W.Sheng, and Y.Li; investigation, T.Chen and A.Ouyang; writing-original draft, T.Chen and H.Zhou; writing-review & editing, T.Chen, A.Ouyang, M.Jin, H.Chen, and H.Zhou; supervision, H.Zhou. All authors reviewed the final manuscript.

Competing interests

The authors declare no competing interests.

Additional information

Supplementary information The online version contains supplementary material available at https://doi.org/10.1038/s41467-025-61587-3.

Correspondence and requests for materials should be addressed to Hongbo Zhou.

Peer review information *Nature Communications* thanks Etori Moreira and the other, anonymous, reviewer(s) for their contribution to the peer review of this work. A peer review file is available.